



# Influences of postproduction heat treatments on the material anisotropy of nickel-aluminum bronze fabricated using wire-arc additive manufacturing process

Chen Shen<sup>1,2</sup> · Gang Mu<sup>1</sup> · Xueming Hua<sup>1</sup> · Fang Li<sup>1</sup> · Dongzhi Luo<sup>2,3</sup> · Xiangru Ji<sup>1</sup> · Chi Zhang<sup>1</sup>

Received: 5 January 2019 / Accepted: 4 April 2019 / Published online: 11 May 2019  
© Springer-Verlag London Ltd., part of Springer Nature 2019

## Abstract

The anisotropy of wire-arc additively deposited nickel-aluminum bronze alloy is studied by microstructure observation and room temperature mechanical property testing. The applied heat treatments have effectively modified the as-fabricated  $\{0\ 1\ 1\} \langle 2\ 1\ 1 \rangle$ ,  $\{1\ 1\ 1\} \langle 1\ 1\ 0 \rangle$  texture into  $\{1\ 1\ 1\}$ . According to the microstructures, the single tempering has resulted in lowest anisotropy while heat treatment with prior homogenization and quenching process induces even intensified annealing textures. However, as shown by the tensile tests, the quenching process is necessary for favorable mechanical properties in the wire-arc additive manufacturing fabricated nickel-aluminum bronze component; therefore, a balance between homogenization annealing and  $\kappa$ -phase precipitation is indicated. Meanwhile, the function of  $\kappa$ -phase precipitates on grain rotation and growth during post-production heat treatment is explained in detail.

**Keywords** Nickel-aluminum bronze · Additive manufacturing · Anisotropy · Grain orientation · Heat treatment

## 1 Introduction

Due to the excellent corrosion-erosion resistances in a seawater environment, nickel-aluminum bronze (NAB) is currently widely used in the maritime industry as key component material (propeller, pump, valve, gland) and surface protection material for steel and aluminum components [1–4]. Currently, NAB components are mostly fabricated by sand mold casting, where porosity is an inevitable problem that reduces physical properties and service performance [5]. Besides the process defects, the cast NAB alloy also has microstructural problems.

The microstructure of cast NAB alloy mainly consists of Widmanstätten  $\alpha$ -phase, Ni-Fe-Al  $\kappa$ -phases, and martensitic  $\beta$ -phase [6]. For cast NAB alloy, the  $\alpha$ -phase coarse grains induced by incidental thick regions during casting would significantly decrease the yield strength; the eutectoid  $\alpha + \kappa_{III}$  structure would induce severe selective phase corrosion; and the retained  $\beta'$ -phase from high-temperature phase region would accelerate the fatigue crack growth. In order to obtain desired microstructure and physical properties, post-production processes such as heat treatment [7], equal channel angular extrusion [8], laser surfacing/cladding [9, 10], thermal spraying [3], and friction stir surfacing [11] have been employed. The mentioned processes can only solve the microstructural problems rather than the porosity process defect. Therefore, a more reliable manufacturing method which can intrinsically reach full density is desired.

In recent years, an additive manufacturing (AM) process based on wire filling and robot-assisted arc deposition, so-called wire-arc additive manufacturing (WAAM) process, has been used to buildup NAB components [12]. Due to the AM nature, WAAM can fabricate component from the CAD environment to an actual part in a completely automatic procedure [13]. Compared with the powder-based AM processes, the cost of WAAM is significantly lower [14]. Therefore,

✉ Xueming Hua  
xmhua@sjtu.edu.cn

<sup>1</sup> Shanghai Key Lab of Materials Laser Processing and Modification, School of Materials Science and Engineering, Shanghai Jiao Tong University, Shanghai 200240, China  
<sup>2</sup> School of Mechanical, Materials and Mechatronics Engineering, Faculty of Engineering and Information Sciences, University of Wollongong, Wollongong, NSW 2522, Australia  
<sup>3</sup> Technical Institute of Ordnance Industry, School of Electrical and Electronic Engineering, Chongqing Electromechanical Vocational Institution, Chongqing 402760, China

currently for maritime industries, WAAM is the only AM process that can be applied. In addition, WAAM is capable of directly manufacturing parts with full density due to the high deposition energy [15]. To date, besides NAB alloy WAAM has been successfully applied to fabricate Ti6Al4V, iron aluminide, titanium aluminide, and copper aluminide [16–21].

Due to the intrinsic good weldability, the free-forming and full density of NAB alloy in WAAM can be easily reached by cold metal transfer (CMT) process. After standard heat treatment, competitive mechanical properties can be obtained in the WAAM-fabricated NAB alloy compared with cast alloy [22]. However, due to the oriented energy deposition during WAAM, the induced material anisotropy leads to orientation-dependent mechanical properties [23]. In the case of NAB alloy, the anisotropy-induced strength difference could reach 40 MPa under as-fabricated condition [24], which causes unreliability in the manufactured part. The interface between two NAB layers contains coarse  $\alpha$ -phase and large martensitic  $\beta'$ -phase which are significantly detrimental to mechanical properties. The most usual method modifying the anisotropy is heat treatment [25]; it has been proved by the previous research that the anisotropy in NAB alloy can be modified using quenching-tempering process. With the increase of tempering temperature, the anisotropy is reduced accordingly. However, the crystallographic mechanism of such modification is not clarified in detail yet.

Anisotropic tensile behavior has continuously been the obstacle blocking metal AM processes being applied in the real industry [12]. In polymer, AM processes such problem can be avoided by directional weaving the plastic wires; therefore, properties in certain orientation can be reinforced [26, 27]. However, the weaving method is literally unacceptable in metal AM processes since the full density is a key requirement. It has been found that the anisotropy of mechanical properties is highly dependent on the texture and can be modified either by adjusting the deposition energy in situ or using post-production heat treatments [28, 29]. And for alloys which contain significant columnar structures induced by AM process such as Ti-based alloys, heat treatment is the effective way of modifying anisotropic properties [30]. Especially for Ti-6.5Al-3.5Mo-1.5Zr-0.3Si, the appropriate heat treatment can transfer the columnar grain structure into entirely equiaxed grains [31]. Therefore, in the current case, investigation on the influence of heat treatment on the texture in the WAAM-fabricated NAB alloy is significant for the further reduction of anisotropic properties in such alloy and the real industry application of WAAM technology.

The present research focuses on the crystallographic mechanism of anisotropy modification in WAAM made NAB alloy component. The role of microstructure in the location- and orientation-dependent properties in WAAM-fabricated NAB is investigated. Since the mechanical properties of WAAM-

fabricated NAB alloy have been studied in detail and that columnar microstructure in the WAAM-deposited NAB has induced a 40-MPa tensile strength difference between longitudinal and normal directions, and the heat treatments can significantly modify the interpass cyclic inhomogeneous microstructure of NAB alloy under as-fabricated condition [24], the aim of this study is rather the characterization of the internal crystallographic structure, and the influences of corresponding heat treatments on the  $\kappa$ -phase precipitates, than the WAAM process optimization.

## 2 Experimental

### 2.1 Sample preparation

Bulk NAB alloy sample was deposited using the robotic WAAM system developed in Shanghai Jiao Tong University. The buildup process was performed using a Yaskawa YR-MA1400 six-axis robot. The deposition power source was chosen as a gas metal arc welding (GMAW) torch using cold metal transfer (CMT) mode (Fronius CMT Advanced 4000 R nc). In the current case, the NAB deposited was built up using commercial 1.2-mm diameter ERCuNiAl welding wire on a 10-mm thick as-cast QAl10-5-5 NAB alloy substrate. Chemical compositions of both the filler wire and substrate are shown in Table 1.

Specific deposition parameters are listed in Table 2. In the present condition, the deposition pass dimensions, width and height, were controlled at 9.5 mm and 0.9 mm respectively. To prevent the multi-layer deposit from collapse, the interpass temperature was controlled at 100 °C. The temperature of the buildup deposit was measured using a K-type thermal couple attached on the substrate with 2 mm from the buildup block. Finally, with 53 layers deposited, a NAB deposit block sized 100 × 100 × 100 mm (length × width × height) was obtained. In addition, the weld passes were planned as a simple zig-zag route in every single layer.

### 2.2 Material assessment

As listed in Table 3, three post-production heat treatments were applied to the as-fabricated material. The designed heat treatments aimed to investigate the influence of quenching process on the tempered NAB alloy, since according to the previous researches, the quench-tempered process can reduce

**Table 1** Compositions of NAB filler wire and substrate (wt%)

	Cu	Al	Ni	Fe	Mn	Si	Zn	Sn	Pb
Wire	Bal.	9.0	4.5	3.5	1.3	0.1	0.02	0.1	0.02
Substrate	Bal.	10	5.0	5.0	1.1	0.25	0.5	0.02	0.05

**Table 2** Deposition parameters of the present WAAM process

Parameters	Unit	Value
Wire feed rate	m/min	7
Deposition rate	kg/h	3.73
Travel speed	mm/min	500
Average current	A	210
Average voltage	V	22
Pure Ar flow rate	L/min	25
Interpass temperature	°C	100
Heat input	J/mm	554

the anisotropy and keep the competitive strength and ductility compared with the as-fabricated condition [24], while the only tempered NAB alloy would lose considerable ductility [22]. The 2-h 900 °C homogenization aimed at removing micro-segregation, internal strength, and local hardness, then water quenching to obtain  $\alpha$ -Cu and  $\alpha + \beta$  phases, which heat treatment method followed by tempering has been proved capable of increasing the tensile strength of the NAB alloy significantly [32]. The standard 6 h of tempering at 675 °C (Def Stan 02-833, 02-747, 02-879) aimed at controlling the microstructure and phase present. Subsequently, the tempered alloys were air cooled to room temperature. Accordingly, the four samples are referred to as the AF (as-fabricated) sample, the Q (quenched) sample, the QT (quench-tempered) sample, and the T (tempered) sample in the present research.

Metallographic samples were ground and finely polished using vibration polishing to remove the surface stress for electron back-scattered diffraction (EBSD) analysis. The sample extraction information and the definition of texture analysis coordinate system are provided in Fig. 1. In the present sample coordinate system, the longitudinal direction (deposition torch travel direction) was set as  $X_0$ ; the normal direction (sample buildup direction) was set as  $Z_0$ , and the transverse direction was set as  $Y_0$ . Metallurgical analysis was performed using a TESCAN® MIRA3 scanning electron microscope (SEM) under back-scattered electron (BSE) mode. And the grain orientation information was obtained using a TESCAN® VEGA3 XMU SEM equipped with an Aztec NordlysMax3 EBSD detector. The step size used for EBSD was 0.5  $\mu\text{m}$ . The EBSD data was collected using Aztec and the acquired EBSD plots were subsequently processed using CHANNEL5 EBSD data processing software.

The macro-phase constituents were characterized using a GBC® MMA X-ray diffractometer (XRD) with  $\text{CuK}\alpha$  radiation ( $\lambda = 1.5418 \text{ \AA}$ ) at a scanning speed of  $2^\circ/\text{min}$ . Vickers hardness was obtained using a load of 1 kg (Hv1) for a 15-s indentation time. Ten indentation points were performed on each sample for the data statistics. Tensile tests were performed on a Zwick® Z100 load unit at a strain rate of  $1.8 \times 10^{-3} \text{ s}^{-1}$  under room temperature. The gauge volume of each

tensile specimen was set as  $4 \times 4 \times 10 \text{ mm}^3$  along the longitudinal ( $X_0$ ) direction of the WAAM sample, which direction has been proved to be the strongest among all the three directions.

## 3 Results

### 3.1 Morphology, hardness and phase constituent

Microstructures of the four samples obtained using SEM under BSE mode are shown in Fig. 2. In the present research, the SEM images are acquired in the longitudinal direction of WAAM deposition. Under BSE mode, the image contrast represents the element weight; the dark precipitates are the  $\kappa$ -phases distributed in the grains and along the grain boundaries. In the AF sample (Fig. 2a), globular  $\kappa_{\text{II}}$ -phases are distributed along the grain boundaries and acicular  $\kappa_{\text{IV}}$ -phase precipitates exist inside the copper grains. Some tiny  $\kappa_{\text{IV}}$ -phase particles can be found distributed along the globular  $\kappa_{\text{II}}$ -phase boundaries with a half micron distance. Besides the  $\kappa$ -phase precipitates, twins can be observed in the microstructure, which are induced by the quenching process in the interface between two deposition layers during the WAAM process. It can be observed that in most of the cases, the acicular  $\kappa_{\text{IV}}$ -phase precipitates are generated along the twins; therefore, the twins can influence the distribution of acicular  $\kappa_{\text{IV}}$ -phase precipitates under non-equilibrium condition.

As shown in Fig. 2 b, the homogenization heat treatment followed by water quenching has entirely transformed the acicular  $\kappa_{\text{IV}}$ -phase precipitates into tiny particles distributed in the  $\beta'$ -phase region. And the size of  $\kappa_{\text{II}}$ -phase is decreased in the Q sample compared with the AF sample. Besides the  $\kappa_{\text{II}}$  and  $\kappa_{\text{IV}}$ -phase,  $\kappa_{\text{III}}$ -phase can also be observed in the  $\beta'$ -phase region while they can be merely found in the AF sample. In addition, large twins can be found in the  $\alpha$ -phase grains in the Q sample, which is due to the water quenching process. Compared with the twins in the AF sample, twins in the Q sample are more integrated with no  $\kappa$ -phase accompanied. When the quenched alloy is further tempered for 6 h (Fig. 2c), the sizes of  $\kappa$ -phases are increased accordingly:  $\kappa_{\text{II}}$ -phase becomes a comparable size as in the AF sample;  $\kappa_{\text{IV}}$ -phase in  $\alpha$ -grains becomes larger while in the residual  $\beta'$ -phase region

**Table 3** Post-production heat treatment conditions of the four cross-sectional samples

Sample no.	Homogenization method	Quenching method	Tempering method
AF	N/A	N/A	N/A
Q	900 °C, 2 h	Water	N/A
QT	900 °C, 2 h	Water	675 °C, 6 h
T	N/A	N/A	675 °C, 6 h

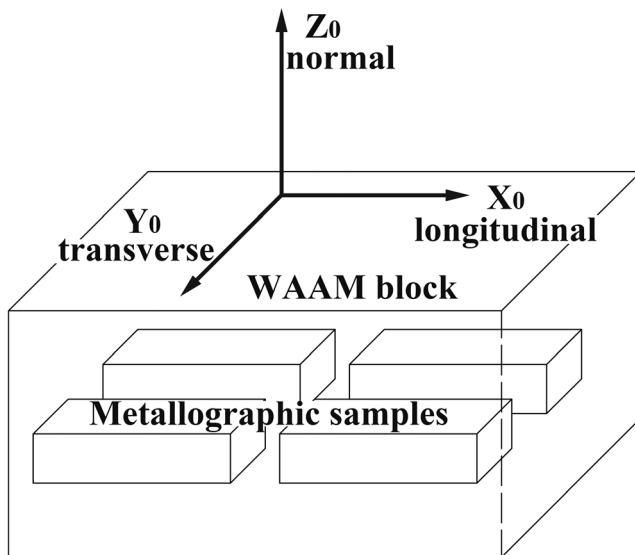


**Fig. 1** Sample extraction locations and EBSD texture analysis coordinate system

$\kappa_{IV}$ -phase stays the same as in the Q sample, and no acicular  $\kappa_{IV}$ -phase is found;  $\kappa_{III}$ -phase performs significant growth by the tempering process. Besides, residual twins can still be observed in the QT sample.

The microstructure of the T sample is shown in Fig. 2 d. Since the alloy is directly tempered from as-fabricated condition at 675 °C for 6 h without the homogenization and quenching process, the iron aluminide-based  $\kappa_{II}$ - and  $\kappa_{IV}$ -phases remain inside the grain with little change. Because as it is known, it usually takes at least 5 to 7 days to transform [25, 33]. Compared with the AF sample, in the T sample significant growth of  $\kappa_{III}$ -phase is performed, since  $\kappa_{III}$ -phase is nickel-based aluminide phase, of which the 675 °C

**Fig. 2** Microstructures of the NAB alloy samples: **a** the AF sample; **b** the Q sample; **c** the QT sample; **d** the T sample

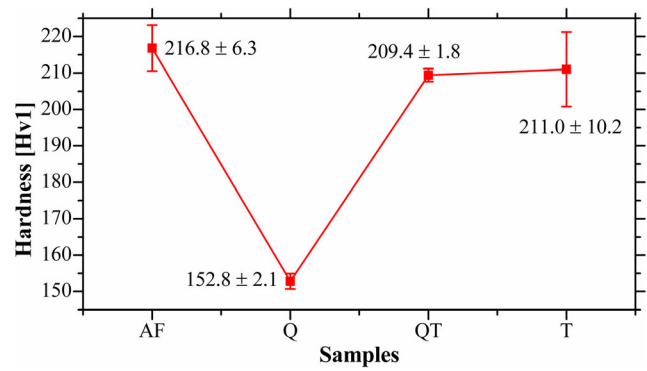
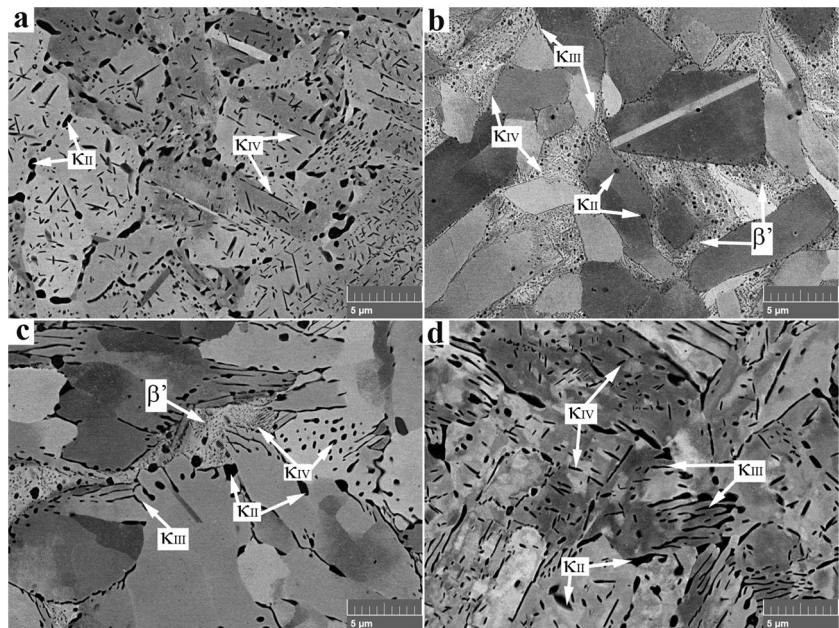


**Fig. 3** Hardness of the NAB alloy samples (over 10 indents have been included for statistics)

tempering temperature is right at the phase growth region according to the binary phase diagram. And compared with the quenched samples, the chemical composition of grains in the T sample is relatively uneven and performs different contrast under the BSE mode.

Hardness data of the four NAB samples is shown in Fig. 3. As can be observed, the most significant influence of the homogenization and quenching process is the reduction of hardness standard deviation in the QT sample compared with the T sample. This is because in the Q sample the AF alloy has already been homogenized; therefore, the separation of  $\kappa$ -phases in the QT sample is much more uniform than the T sample, thus making the hardness more stable. And with the addition of tempering, hardness of the QT sample is increased from the quenched state and becomes competitive to the AF and T sample. Such a phenomenon is inclined to the microstructure change: the significant hardness decrease in the Q sample is caused by the absorption of  $\kappa$ -phases into  $\alpha$ -grains; with further tempering,  $\kappa$ -phases separate out from  $\alpha$ -grains



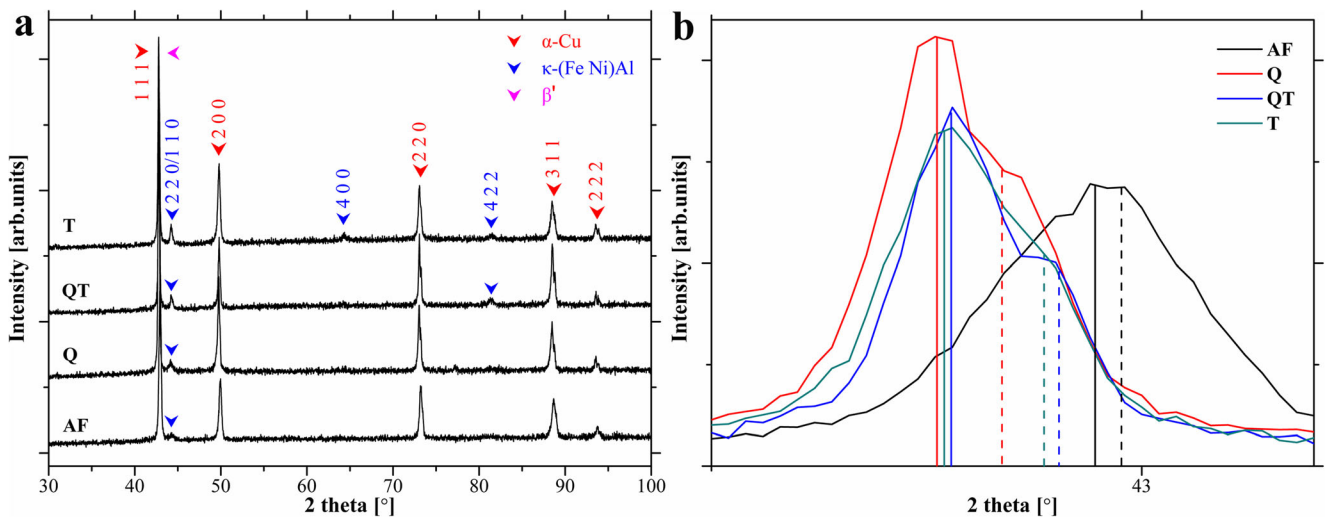


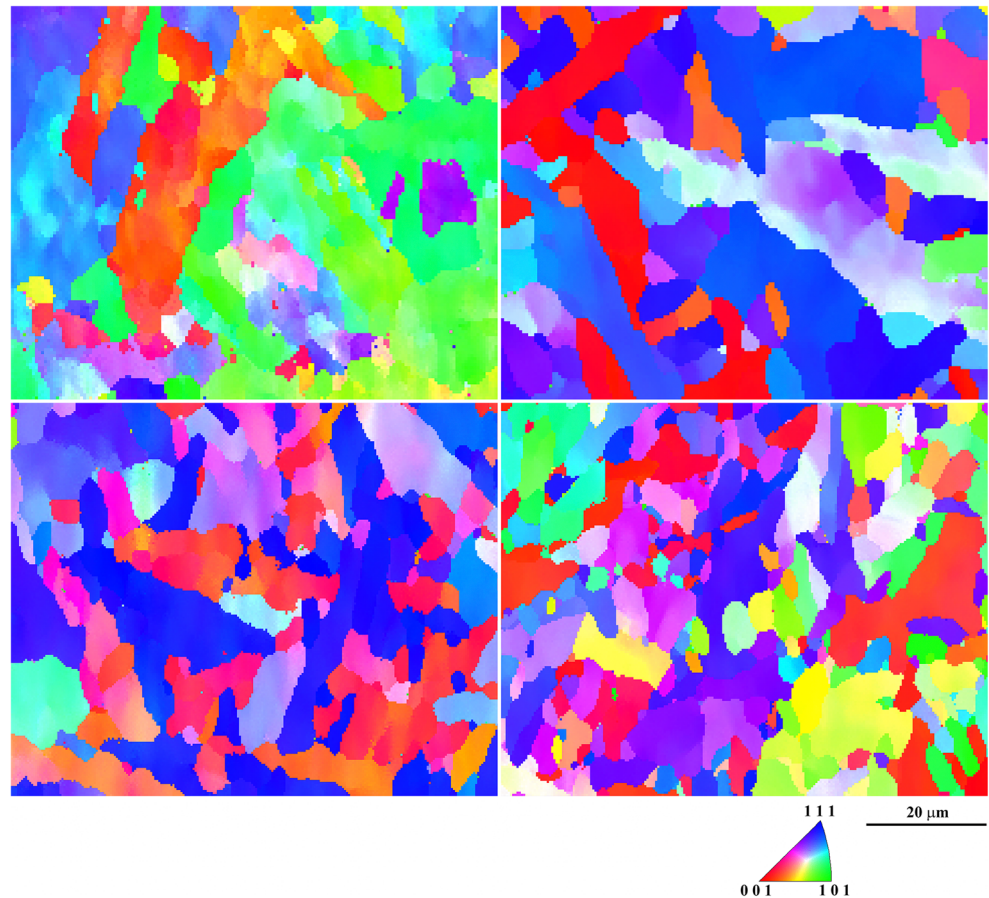
**Fig. 4** XRD patterns of the NAB alloy samples: **a** diffraction patterns of all reflections from 30 to 100°; **b** magnified 1 1 1 reflection of  $\alpha$ -phase; solid lines are the main peak positions and dash lines are the secondary peak positions (peak fitted using the Gauss algorithm)

and grow, thus increasing the average hardness back to the original state; however, without the homogenization process, the microstructure stays almost the same; therefore, the hardness stays as well.

X-ray diffraction patterns of the four NAB samples are shown in Fig. 4. Generally, according to Fig. 4 a, the heat

treatments have not influenced the peak intensity too much, but with the tempering process, iron/nickel aluminide  $\kappa$ -phases at 4 0 0 and 4 2 2 reflections have appeared in the QT and T samples which indicates the growth of  $\kappa$ -phases during the tempering process. The  $\kappa$ -phase dissolving can be revealed by the peak shifting of 1 1 1 reflection of  $\alpha$ -phase

**Fig. 5** EBSD IPF maps of  $\alpha$ -phase grains in the NAB alloy samples: **a** the AF sample; **b** the Q sample; **c** the QT sample; **d** the T sample



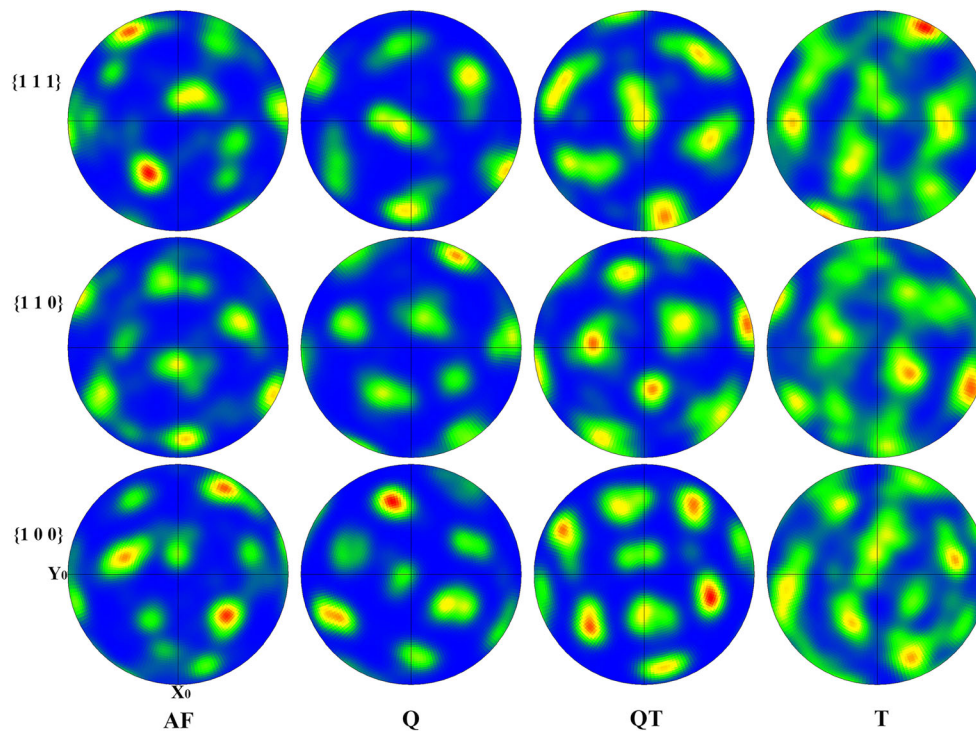


**Fig. 6**  $\alpha$ -Phase pole figures of the XOY section in the four NAB samples

which is shown in Fig. 4 b. Since Al has larger atom radius than Fe and Ni, the solid lines (main peak) represent the Al solid solution, and dashed lines (secondary peak) represent the Fe and Ni solution. As can be observed, the homogenization and quenching process has dissolved relatively more  $\kappa$ -phases than the other three samples; therefore, the main peak and secondary peak at 1 1 1 reflection have moved to  $42.749^\circ$  ( $d = 2.11362 \text{ \AA}$ ) and  $42.854^\circ$  ( $d = 2.10851 \text{ \AA}$ ) respectively, which result is consistent with the SEM observation. With further tempering process,  $\kappa$ -phases start to separate out; therefore, the secondary peak of the QT sample moves to  $42.915^\circ$  ( $d = 2.11082 \text{ \AA}$ ), while the main peak stays relatively still. Without the homogenization and quenching process, in the T sample, the tempering process directly absorbed the  $\kappa$ -phases, thus moving the main and secondary peaks to  $42.773^\circ$  ( $d = 2.11232 \text{ \AA}$ ) and  $42.902^\circ$  ( $d = 2.11157 \text{ \AA}$ ) respectively, from their original spacings in the AF sample. Generally, although from different paths, the QT and T samples reach almost same interplanar spacings.

### 3.2 Grain orientation analysis

EBSD inverse pole figure (IPF) maps of  $\alpha$ -grains in the four samples are shown in Fig. 5. As can be observed from Fig. 5 a, in the AF sample, the grains are dominated in  $\langle 1 0 1 \rangle$  and  $\langle 1 1 1 \rangle$  directions. And the T sample has shown relatively inherited grain orientations from the AF sample. When the homogenization heat treatment is applied to the as-fabricated alloy, most of the grains turn to  $\langle 1 1 1 \rangle$  and  $\langle 0 0 1 \rangle$  rather

than  $\langle 1 0 1 \rangle$  in the Q sample. Subsequently, with the further tempering process, the grains are refined and further turn to  $\langle 1 1 1 \rangle$  direction in the QT sample.

Pole figures of the four NAB samples are shown in Fig. 6: the AF sample shows  $\{1 1 1\} \langle 1 1 0 \rangle$  texture, the Q and QT samples show strong  $\{1 1 1\}$  texture, and the T sample shows a relatively isotropic lattice plane distribution. The  $\{1 1 1\}$  texture in the Q samples is the annealing texture induced by the homogenization process. At the  $900^\circ\text{C}$  temperature, the  $\kappa$ -phases have been decomposed and absorbed into the  $\alpha$ -grains; thus, the grains are no longer limited by the  $\kappa$ -phases precipitates; therefore, the grains are transformed into their prior growing orientation. Subsequently, the QT sample inherits the  $\{1 1 1\}$  texture from the Q sample and further evolves to a stronger  $\{1 1 1\}$  texture. The T sample is evolved from the AF sample by tempering process; thus, there is some residual  $\{1 1 1\} \langle 1 1 0 \rangle$  texture but with very weak relative intensity. This is because the grains are pinned by the  $\kappa$ -phases precipitates; therefore, the grain growth is relatively isotropic compared with the Q and QT sample.

Grain orientations are further counted by inverse pole figures shown in Fig. 7. Generally, grains of the AF sample exhibit  $\langle 1 1 1 \rangle$  in the  $Y_0$  direction and some  $\langle 1 1 0 \rangle$  in the  $Z_0$  direction which explains the appearance of  $\{1 1 1\} \langle 1 1 0 \rangle$  texture in Fig. 6. After the homogenization and quenching process, orientation concentration of the grains in the Q sample exhibits relatively multi-directional and performs  $\langle 1 1 1 \rangle$  in  $Z_0$  direction,  $\langle 1 1 0 \rangle$  in the  $Y_0$  direction, and  $\langle 1 1 2 \rangle$  in the  $X_0$  direction. Subsequently, with the further tempering

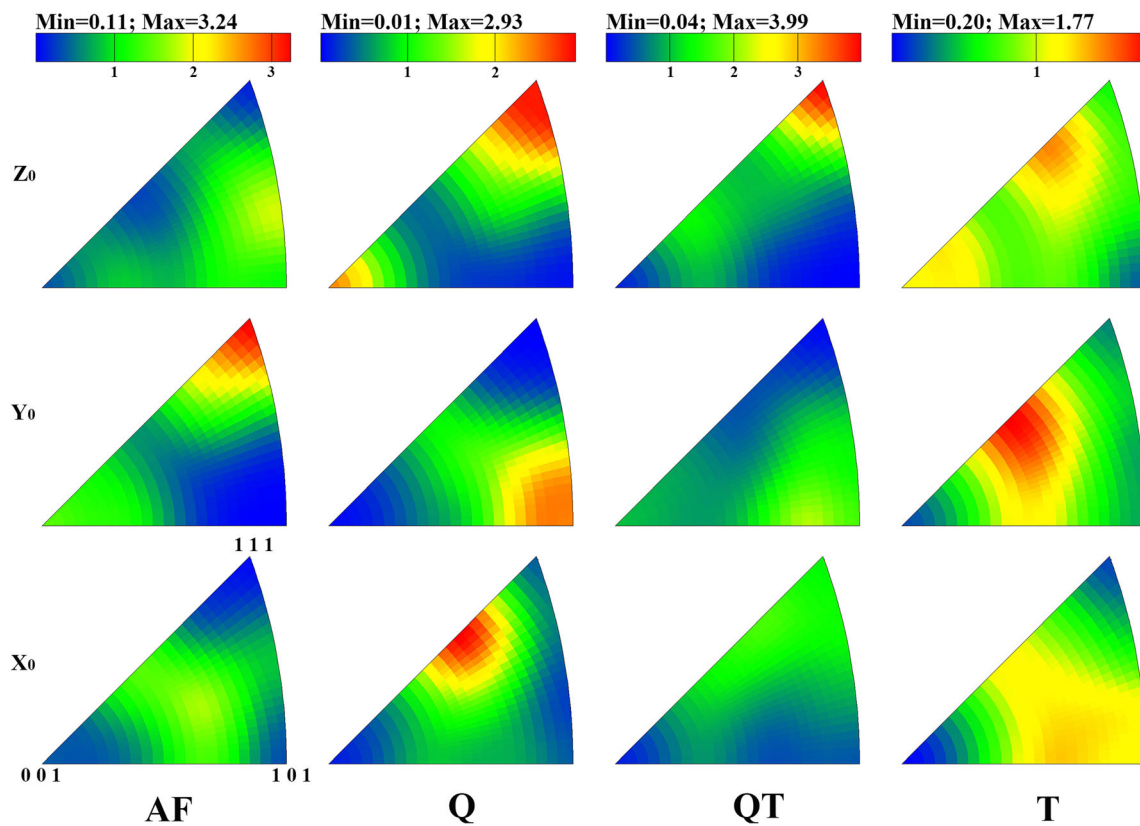


Fig. 7 Inverse pole figures of the four NAB samples in  $X_0$ ,  $Y_0$ , and  $Z_0$  directions

process, grains in the QT sample show notorious  $\langle 1\ 1\ 1 \rangle$  in the  $Z_0$  direction with some  $\langle 1\ 1\ 0 \rangle$  in the  $Y_0$  direction. When the NAB alloy is tempered without the homogenization and quenching process, as shown by the T sample, the grain orientations show a relatively isotropic distribution compared with the previous three samples. In addition, according to the obtained grain orientation concentration densities, the QT sample shows the highest concentration density and the T samples shows the lowest density; therefore, the anisotropy of the NAB sample is weakest in the T sample as anisotropy is positively correlated with the texture intensity.

Orientation distribution function (ODF) maps of the four NAB samples are shown in Fig. 8: the AF sample exhibits a strong  $\{1\ 1\ 1\} \langle 1\ 1\ 0 \rangle$  texture with some  $\{0\ 1\ 1\} \langle 2\ 1\ 1 \rangle$  shown in  $\varphi_2 = 0^\circ$ ; the Q and QT samples exhibit intensified  $\{1\ 1\ 1\} \langle 1\ 1\ 0 \rangle$  and  $\{1\ 1\ 1\} \langle 1\ 1\ 2 \rangle$  textures, and the Q sample additionally exhibits a mild  $\{0\ 0\ 1\} \langle 1\ 1\ 0 \rangle$  texture, as the Q sample is directly water quenched from the 2-h 900 °C annealing; the T sample shows copper type  $\{1\ 1\ 2\} \langle 1\ 1\ 1 \rangle$  texture in  $\varphi_2 = 45^\circ$  and some rotated cube  $\{0\ 0\ 1\} \langle 1\ 1\ 0 \rangle$  texture but with low intensity.

As it is known, texture roughly has 20–50% effect on the intrinsic properties of manufactured specimens such as elastic modulus, Poisson’s ratio, and mechanical properties [34–37]. Yuan et al. [34] studied the tensile behavior of friction stir

welding (FSW) processed magnesium alloy with strong basal texture and showed that strong tensile anisotropy exists in longitudinal and transverse directions. Due to the variation of directional grain growth in longitudinal and normal directions, the typical characteristic of AM is the tensile anisotropy in such orientations [38]. However, in the present case, the acicular  $\kappa_{IV}$ -precipitates in the AF sample generated during deposition considerably pinned the grains; therefore, the AF sample shows a deformed  $\{0\ 1\ 1\} \langle 2\ 1\ 1 \rangle$  with  $\{1\ 1\ 1\} \langle 1\ 1\ 0 \rangle$ .

After the as-fabricated alloy being annealed, the induced grain rotation and recrystallization mitigate and transmit the  $\{0\ 1\ 1\} \langle 2\ 1\ 1 \rangle$  texture to  $\{1\ 1\ 1\} \langle 1\ 1\ 0 \rangle$  and  $\{1\ 1\ 1\} \langle 1\ 1\ 2 \rangle$  in the Q and QT samples, of which textures  $\{1\ 1\ 1\}$  plane is the preferential orientation, as the close-packed  $\{1\ 1\ 1\}$  plane in fcc structure provides less obstacles for dislocations motion during processing [39, 40]. And the T sample shows some  $\{1\ 1\ 1\} \langle 1\ 1\ 0 \rangle$  but with low intensity. All the heat-treated samples show  $\{1\ 1\ 1\}$  texture, but vary in intensity. The variation can be explained via grain coalescence [41, 42] and grain boundary migration [43, 44]: the T sample has a higher volume of precipitates to pin the dislocation motions and further grain boundary dislocations to pile up at boundary or climbing along grain boundary, thus having an effective way to hinder the grain rotation; on the other hand, the Q and QT samples



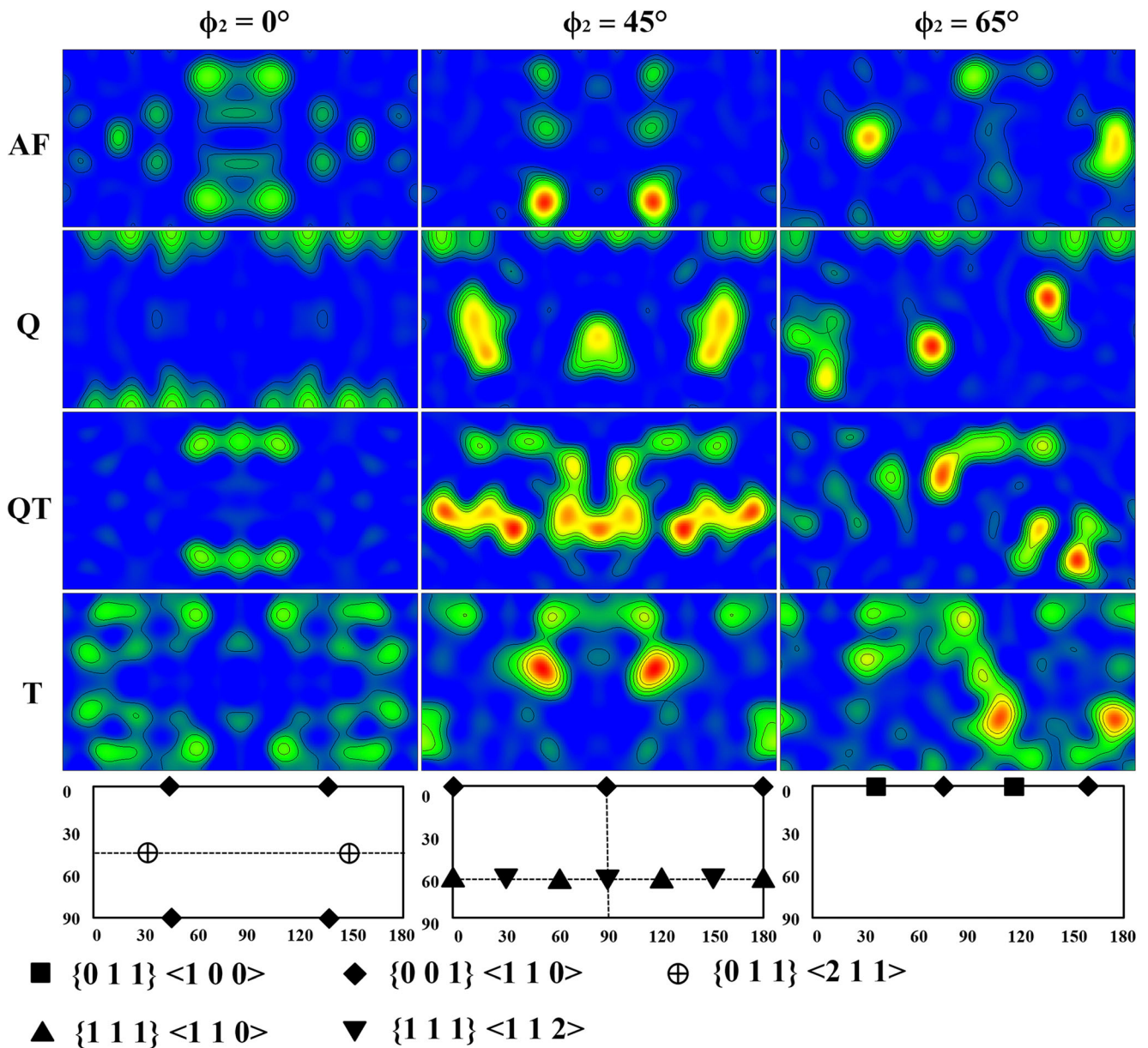


**Fig. 8** Orientation distribution function maps of the four NAB samples at  $\phi_2 = 0^\circ$ ,  $45^\circ$ , and  $65^\circ$ . Ideal texture locations at the corresponding  $\phi_2$  Euler angles are indicated using schematic drawings

which have experienced the solid solution process of  $\kappa$ -phases have a rather flexibility of nucleation and grain growth, therefore presenting higher  $\{1\ 1\ 1\}$  annealing texture intensities.

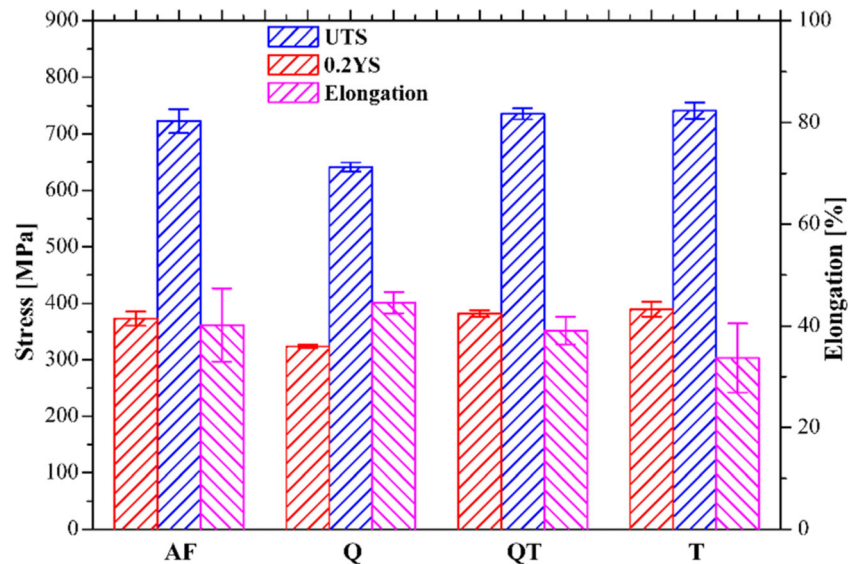
### 3.3 Tensile test

Room temperature tensile properties of the NAB alloy with post-production heat treatments are shown in Fig. 9 and Table 4. Generally, the AF, QT, and T samples show similar strength while the strength of the Q sample is much lower. This is because of the solid solution of the  $\kappa$ -phase elements into the  $\alpha$ -grains during the  $900^\circ\text{C}$  annealing process. On the

other hand, with the homogenization heat treatment, the stability of tensile strengths and ductility increases as shown by the smaller scale bar compared with the AF and T samples. As compared the QT sample with the T sample, similar strength and higher ductility have been obtained by the quenching-tempering process, therefore the QT sample is more favorable in tensile properties. As can be observed in the tensile properties of Q and QT sample, with more  $\kappa$ -precipitates separate out in the sample, higher strength is obtained but induces lower ductility. In addition, the single tempering process applies little effect on the tensile stability but increases strength and decreases ductility as compared with the AF sample.



**Fig. 9** Tensile results of the as-fabricated (AF), quenched (Q), quenched-tempered (QT), and tempered (T) nickel-aluminum bronze samples



## 4 Discussion

As shown by the experimental results, favorable mechanical properties are obtained in the QT sample while low anisotropy is obtained in the T sample. The quenching process has decomposed the  $\kappa$ -phases into the  $\alpha$ -grains; therefore, in the microstructure of the QT sample which inherited from the Q sample, the original acicular  $\kappa_{IV}$ -phase precipitates are separated out as globular and the  $\alpha$ -grains are comparatively clean. The uniformed color contrast in the grains indicated the homogenized composition due to the high-temperature annealing. The relatively reduced segregation by the heat treatments is shown in the XRD results, as 1 1 1 reflection of the  $\alpha$ -phase in heat-treated samples moves to larger  $d$ -spacing than the AF sample, which phenomenon indicates the dissolve of  $\kappa$ -phases. However, the absorption of precipitates on the other hand removes the limitation on the grain rotation and growth during annealing, thus inducing annealing texture.

In the EBSD results, strong annealing texture  $\{1\ 1\ 1\}$  is observed in the Q and QT samples, while the T sample simply inherits the residual  $\{1\ 1\ 1\}$   $\langle 1\ 1\ 0 \rangle$  texture from the AF sample but with very low intensity. Furthermore, as can be observed from the inverse pole figures in Fig. 7, due to the

900 °C annealing and water quenching, the precipitate limitations are fully removed in the Q sample; therefore, the grains freely rotate and grow to the fcc orientations  $\langle 1\ 1\ 1 \rangle$ ,  $\langle 1\ 1\ 0 \rangle$ , and  $\langle 1\ 1\ 2 \rangle$ . With further 675 °C annealing, the  $\kappa$ -phases rather are separated out at the grain boundaries in the T sample than inside the grains; in such case, the grains can still grow and rotate. Since the preferential grain growth orientation for fcc structure is  $\langle 1\ 1\ 1 \rangle$ , the grains further turn to  $\langle 1\ 1\ 1 \rangle$  while the growth in the other two directions mitigates; therefore, the T sample shows a further intensified  $\{1\ 1\ 1\}$  texture. On the other hand, in the case when the 675 °C annealing is directly applied to the as-fabricated component without the 900 °C annealing (the T sample), since such temperature cannot dissolve the  $\kappa$ -phases, the grain rotation is restricted by both the original  $\kappa_{II}/\kappa_{IV}$ -phases and newly generated  $\kappa_{III}$ -phase; therefore, the grain growth is relatively limited in the original orientation. Also, due to the guide of disorganized acicular  $\kappa$ -precipitate, the  $\{1\ 1\ 1\}$   $\langle 1\ 1\ 0 \rangle$  texture inherited from the AF sample is further decreased.

According to the ODF maps in Fig. 8, the dominating textures in the Q and QT samples are  $\{1\ 1\ 1\}$   $\langle 1\ 1\ 0 \rangle$  with small amount of  $\{1\ 1\ 1\}$   $\langle 1\ 1\ 2 \rangle$ , while the textures in the AF sample are some weak  $\{1\ 1\ 1\}$   $\langle 1\ 1\ 0 \rangle$  and  $\{0\ 1\ 1\}$   $\langle 2\ 1\ 1 \rangle$ . As it is known,  $\{1\ 1\ 1\}$   $\langle 1\ 1\ 0 \rangle$  is the typical annealing texture of Cu-based alloys while  $\{1\ 1\ 1\}$   $\langle 1\ 1\ 2 \rangle$  and  $\{0\ 1\ 1\}$   $\langle 2\ 1\ 1 \rangle$  are the typical deformation textures of Cu-based alloys. The appearance of  $\{1\ 1\ 1\}$   $\langle 1\ 1\ 0 \rangle$  in the AF sample is because the multi-layer deposition during WAAM process can be considered as a multi-annealing process on the buildup metal, which also can be indicated by the appearance of annealing twins in the AF sample. And the appearance of  $\{1\ 1\ 1\}$   $\langle 1\ 1\ 2 \rangle$  in the Q and QT sample is caused rather by the grain rotation than growth during the 900 °C annealing, since the formation of

**Table 4** The ultimate tensile strength (UTS), 0.2 yield strength (0.2YS), and elongation of the as-fabricated (AF), quenched (Q), quenched-tempered (QT), and tempered (T) nickel-aluminum bronze samples

	AF	Q	QT	T
UTS	722.9 ± 21.3	641.4 ± 8.1	735.6 ± 9.7	741.1 ± 14.3
0.2YS	373.1 ± 12.6	323.8 ± 2.7	381.9 ± 5.9	389.5 ± 13.3
Elongation	40.2 ± 7.2	44.6 ± 2.1	39.1 ± 3.3	33.7 ± 6.8

{1 1 1} <1 1 2> is paused in the further 675 °C annealing, in which case the  $\alpha$ -grain continues to grow and recrystallize.

In the present case, the applied annealing processes have significantly modified the as-fabricated microstructure and texture. The 900 °C annealing and quenching have brought strong {1 1 1} annealing texture in the final QT sample while the T sample shows a favorable isotropic grain orientation state, which phenomenon makes the high-temperature annealing reductant. However, as shown by the hardness and tensile test, the QT sample shows favorable mechanical properties with higher ductility and stability than the T sample. From the point of mechanical properties, the 900 °C annealing is still necessary to obtain better ductility and stability. Although intensified annealing texture is found in the Q and QT sample, the {1 1 1} texture is rather induced by the post-production heat treatment than the AM process. From this point of view, the original AM-induced anisotropy has already been transferred. Therefore, the existence of a balance between high-temperature annealing and medium temperature annealing can be confirmed, by which heat treatment the  $\kappa$ -phases shall be partially dissolved with little change of grain rotation and growth in the first step, then the  $\kappa$ -phases be further separated out along with grain recrystallizations in the subsequent step.

## 5 Conclusion

The intent of present work has been to investigate the influence of post-production heat treatment on the anisotropy in the wire-arc additive manufacturing–fabricated nickel-aluminum bronze part and to find the relationship between mechanical properties and modified anisotropy. The following conclusions can be drawn:

1. For NAB alloy in the present case, the original anisotropic microstructure induced by the wire-arc additive manufacturing process can be effectively modified by the applied heat treatment. However, the quenched and quenched-tempered processes have induced inordinate grain rotation and growth, thus causing intensified {1 1 1} annealing texture compared with the as-fabricated sample. On the other hand, the single tempering process shows relatively isotropic grain orientations, since the  $\kappa$ -phases significantly influence the grain rotation and growth during heat treatment, especially the acicular  $\kappa_{IV}$ -precipitates.
2. The  $\kappa$ -phases distributed in the  $\alpha$ -grain and grain boundary significantly influence the stability of mechanical properties. The 6-h 675 °C tempering process shows little effect on the original WAAM-induced mechanical instability, since the tempering method has little effect on Fe-Al phase but can cultivate the Ni-Al-based  $\kappa_{III}$ -phase. Because the tempering temperature is right at the phase growth region in the Ni-Al binary phase diagram. Therefore, the tempered sample shows higher strength, but lower ductility compared with the as-fabricated sample. When the quenching process is applied, the  $\kappa$ -phases are entirely dissolved into the  $\alpha$ -grains and separated out uniformly in the subsequent tempering process, which leads to a more stabilized tensile properties and higher ductility with similar strength. Therefore, the quenching process is still necessary for favorable tensile properties in the wire-arc additive manufacturing–fabricated nickel-aluminum bronze component.
3. The existence of a balance between high-temperature annealing and medium temperature annealing can be confirmed. The ideal heat treatment should partially dissolve the  $\kappa$ -phases with little change of grain rotation and growth in the quenching step, then further separating the  $\kappa$ -phases out along with grain recrystallizations in the tempering step. Thus, both isotropic microstructure and favorable mechanical properties can be reached.

**Acknowledgments** Gratitude is also due to the Instrumental Analysis Center of Shanghai Jiao Tong University for the microstructure tests.

**Funding information** The authors acknowledge the support of the National Key Research and Development Program of China [Grant No.: 2016YFB0301205] and “Sailing Program” of Shanghai Science and Technology Committee [Grant No.: 19YF1422700].

**Data availability** The raw/processed data required to reproduce these findings cannot be shared at this time as the data also forms part of an ongoing study.

## References

1. Jahanafrooz A, Hasan F, Lorimer GW, Ridley N (1983) Microstructural development in complex nickel-aluminum bronzes. *Metall Trans A* 14:1951–1956
2. Tan KS, Wharton JA, Wood RJK (2005) Solid particle erosion–corrosion behaviour of a novel HVOF nickel aluminium bronze coating for marine applications—correlation between mass loss and electrochemical measurements. *Wear* 258:629–640
3. Barik RC, Wharton JA, Wood RJK, Tan KS, Stokes KR (2005) Erosion and erosion–corrosion performance of cast and thermally sprayed nickel–aluminium bronze. *Wear* 259:230–242
4. Liu Y, Mochel ME, Mazumder J, Shibata K (1994) TEM study of precipitates in laser clad Ni Al bronze. *Acta Metall Mater* 42:1763–1768
5. Ferrara RJ, Caton T (1982) Review of dealloying of cast aluminum bronze and nickel-aluminum bronze alloys in sea water service. *Mater Perform* 21:30–34
6. Culpan EA, Rose G (1978) Microstructural characterization of cast nickel aluminium bronze. *J Mater Sci* 13:1647–1657
7. Olszewski AM (2008) Dealloying of a nickel–aluminum bronze impeller. *J Fail Anal Prevent* 8:505–508
8. Al-Hashem A, Cacer PG, Riad WT, Shalaby HM (1995) Cavitation corrosion behavior of cast nickel-aluminum bronze in seawater. *Corrosion* 51:331–342

9. Tang CH, Cheng FT, Man HC (2004) Effect of laser surface melting on the corrosion and cavitation erosion behaviors of a manganese–nickel–aluminium bronze. *Mater Sci Eng A* 373:195–203
10. Hyatt CV, Magee KH, Betancourt T (1998) The effect of heat input on the microstructure and properties of nickel aluminum bronze laser clad with a consumable of composition Cu-9.0 Al-4.6 Ni-3.9 Fe-1.2 Mn. *Metal Mater Trans A* 29:1677–1690
11. Hanke S, Fischer A, Beyer M, Dos-Santos J (2011) Cavitation erosion of NiAl-bronze layers generated by friction surfacing. *Wear* 273:32–37
12. Frazier WE (2014) Metal additive manufacturing: a review. *J Mater Eng Perform* 23:1917–1928
13. Ding D, Pan Z, Cuiuri D, Li H (2015) A practical path planning methodology for wire and arc additive manufacturing of thin-walled structures. *Robot Cim-int Manuf* 34:8–19
14. Ding D, Pan Z, Cuiuri D, Li H (2015) A multi-bead overlapping model for robotic wire and arc additive manufacturing (WAAM). *Robot Cim-int Manuf* 31:101–110
15. Ding D, Pan Z, Cuiuri D, Li H (2015) Wire-feed additive manufacturing of metal components: technologies, developments and future interests. *Int J Adv Manuf Tech* 81:465–481
16. Wang F, Williams S, Rush M (2011) Morphology investigation on direct current pulsed gas tungsten arc welded additive layer manufactured Ti6Al4V alloy. *Int J Adv Manuf Tech* 57:597–603
17. Brandl E, Michailov V, Viehweger B, Leyens C (2011) Deposition of Ti-6Al-4 V using laser and wire, part I: microstructural properties of single beads. *Surf Coat Technol* 206:1130–1141
18. Ma Y (2015) Fabrication of gamma titanium aluminide alloys by gas tungsten arc welding-based additive layer manufacturing. University of Wollongong
19. Shen C, Pan Z, Ma Y, Cuiuri D, Li H (2015) Fabrication of iron-rich Fe–Al intermetallics using the wire-arc additive manufacturing process. *Addit Manuf* 7:20–26
20. Shen C, Pan Z, Cuiuri D, Roberts J, Li H (2016) Fabrication of Fe-Fe-Al functionally graded material using the wire-arc additive manufacturing process. *Metal Mater Trans B* 47:763–772
21. Dong B, Pan Z, Shen C, Ma Y, Li H (2017) Fabrication of copper-rich Cu-Al alloy using the wire-arc additive manufacturing process. *Metal Mater Trans B* 48:3143–3151
22. Ding D, Pan Z, van Duin S, Li H, Shen C (2016) Fabricating superior nial bronze components through wire arc additive manufacturing. *Materials* 9:652
23. Shen C, Pan Z, Cuiuri D, Dong B, Li H (2016) In-depth study of the mechanical properties for Fe3Al based iron aluminide fabricated using the wire-arc additive manufacturing process. *Mater Sci Eng A* 669:118–126
24. Shen C, Pan Z, Ding D, Lei Y, Nie N, Luo D, Cuiuri D, van Duin S, Li H (2018) The influence of post-production heat treatment on the multi-directional properties of nickel-aluminum bronze alloy fabricated using wire-arc additive manufacturing process. *Addit Manuf* 23:411–421
25. Shen C, Pan Z, Cuiuri D, van Duin S, Luo D, Dong B, Li H (2018) Influences of postproduction heat treatment on Fe3Al-based iron aluminide fabricated using the wire-arc additive manufacturing process. *Int J Adv Manuf Technol* 97:335–344
26. Torrado AR, Shemelya CM, English JD, Lin Y, Wicker RB, Roberson DA (2015) Characterizing the effect of additives to ABS on the mechanical property anisotropy of specimens fabricated by material extrusion 3D printing. *Addit Manuf* 6:16–29
27. Quan Z, Wu A, Keefe M, Qin X, Yu J, Suhr J, Byun JH, Kim BS, Chou TW (2015) Additive manufacturing of multi-directional preforms for composites: opportunities and challenges. *Mater Today* 18:503–512
28. Popovich VA, Borisov EV, Popovich AA, Sufiarov VS, Masaylo DV, Alzina L (2017) Functionally graded Inconel 718 processed by additive manufacturing: crystallographic texture, anisotropy of microstructure and mechanical properties. *Mater Des* 114:441–449
29. Carroll BE, Palmer TA, Beese AM (2015) Anisotropic tensile behavior of Ti–6Al–4V components fabricated with directed energy deposition additive manufacturing. *Acta Mater* 87:309–320
30. Zhu Y, Liu D, Tian X, Tang H, Wang H (2014) Characterization of microstructure and mechanical properties of laser melting deposited Ti–6.5 Al–3.5 Mo–1.5 Zr–0.3 Si titanium alloy. *Mater Des* 56:445–453
31. Zhu Y, Tian X, Li J, Wang H (2015) The anisotropy of laser melting deposition additive manufacturing Ti–6.5 Al–3.5 Mo–1.5 Zr–0.3 Si titanium alloy. *Mater Des* 67:538–542
32. Kaplan M, Yildiz A (2003) The effects of production methods on the microstructures and mechanical properties of an aluminum bronze. *Mater Lett* 57:4402–4411
33. McKamey CG (1996) Iron aluminides. In: *Physical metallurgy and processing of intermetallic compounds*. Springer, Boston, pp 351–391
34. Yuan W, Mishra RS, Carlson B, Mishra RK, Verma R, Kubic R (2011) Effect of texture on the mechanical behavior of ultrafine grained magnesium alloy. *Scr Mater* 64:580–583
35. Faurie D, Renalt PO, Le Bourhis E, Goudeau P (2006) Study of texture effect on elastic properties of Au thin films by X-ray diffraction and in situ tensile testing. *Acta Mater* 54:4503–4513
36. Hoseini M, Shahryari A, Omanovic S, Szpunar JA (2009) Comparative effect of grain size and texture on the corrosion behaviour of commercially pure titanium processed by equal channel angular pressing. *Corros Sci* 51:3064–3067
37. Wu L, Agnew SR, Ren Y, Brown DW, Clausen B, Stoica GM, Wenk HR, Liaw PK (2010) The effects of texture and extension twinning on the low-cycle fatigue behavior of a rolled magnesium alloy, AZ31B. *Mater Sci Eng A* 527:7057–7067
38. Pal S, Lojen G, Kokol V, Drstvensek I (2018) Evolution of metallurgical properties of Ti-6Al-4V alloy fabricated in different energy densities in the selective laser melting technique. *J Manuf Process* 35:538–546
39. Wang L, Teng J, Liu P, Hirata A, Ma E, Zhang Z, Chen M, Han X (2014) Grain rotation mediated by grain boundary dislocations in nanocrystalline platinum. *Nat Commun* 5:4402
40. Allen CW, Rehn LE (1989) Irradiation-induced grain growth: role of dislocations. *MRS Online Proceedings Library Archive* 157
41. Zhang Y, Tucker GJ, Trelewicz JR (2017) Stress-assisted grain growth in nanocrystalline metals: grain boundary mediated mechanisms and stabilization through alloying. *Acta Mater* 131:39–47
42. Feltham P (1957) Grain growth in metals. *Acta Metall* 5:97–105
43. Kacher J, Robertson IM, Nowell M, Knapp J, Hattar K (2011) Study of rapid grain boundary migration in a nanocrystalline Ni thin film. *Mater Sci Eng A* 528:1628–1635
44. Bozzolo N, Agnoli A, Souai N, Bernacki M, Loge RE (2013) Strain induced abnormal grain growth in nickel base superalloys. *Mater Sci Forum* 753:321–324

**Publisher's note** Springer Nature remains neutral with regard to jurisdictional claims in published maps and institutional affiliations.